Acta Materialia 273 (2024) 119958

Contents lists available at ScienceDirect

Acta Materialia

journal homepage: www.elsevier.com/locate/actamat

Resolving the long-standing discrepancy in Fe_3Al ordering mobilities: A synergistic experimental and phase-field study

Yuheng Liu [a], Madoka Watanabe [a], Masayuki Okugawa [a,*], Takashi Hagiwara [a], Tsubasa Sato [a], Yusuke Seguchi [a], Yoshitaka Adachi [b], Yoritoshi Minamino [a], Yuichiro Koizumi [a,*]

[a] Graduate School of Engineering, Osaka University, 2-1 Yamadaoka, Suita 565-0871, Japan
[b] Department of Material Design Innovation Engineering, Nagoya University, Nagoya 464-8603, Japan

ARTICLE INFO

Keywords:
Phase-field simulation
Transmission electron microscopy
Ordering mobility
Antiphase boundary
Fe_3Al

ABSTRACT

This study addressed the long-standing challenge of determining the growth kinetic of Antiphase Domains (APDs) with $D0_3$-ordered structure in Fe_3Al by the combination of phase-field (PF) simulations and transmission electron microscopy (TEM) observation. The "shape coefficient" which correlates the growth rate of APD with 3-dimensional intricate shape and the shrinking rate of 2-dimensional circular antiphase boundaries (APBs) in thin film was assessed through a comparative analysis of PF simulations involving the shrinking of 2D circular APBs and the growth of 3D APDs emerged from a disordered state. Simultaneously, the increase rate in APD size in bulk samples after heat treatment was measured using TEM. By incorporating the calculated shape coefficient and experimental data on APD growth rates, we successfully derived accurate values of mobility for forming $D0_3$ type ordered structure. The ordering mobilities evaluated by this approach align more closely with those obtained through traditional X-ray powder diffraction of order-order relaxation rather than those obtained through in-situ TEM observation. This finding lays the foundation for optimizing heat treatment conditions to regulate APD structure and enhance the superelasticity of Fe_3Al primarily due to the interaction between dislocation and APBs. This methodology can be extended to estimate the ordering mobility of other intermetallic.

1. Introduction

Intermetallic compounds possessing ordered structures find applications as specialized structural or functional materials due to their unique mechanical [1], chemical [2], electrical [3], and magnetic properties [4]. In the early stages of developing ordered structures, regions containing atoms arranged in an ordered way with the same crystallographic orientation, known as ordered domains or antiphase domains (APDs), are initially formed. When multiple APDs expand and intersect with adjacent ones, they merge if their orientations are consistent. However, if the orientations differ, a less regular boundary known as the antiphase boundary (APB) is formed. The characteristic properties of the ordered intermetallic are closely linked to the size of the APD or the density of the APBs [5–11]. For instance, the critical resolved shear stress (CRSS) for prism slips in $D0_{19}$-ordered Ti_3Al with fine APDs of approximately 30 nm is approximately six times larger than that of single-domain crystals [5]. Another example is the superelasticity of Fe_3Al [7,9]. Fe_3Al alloys with $D0_3$-ordered structures have been developed as an alternative to stainless steel [12], and superelasticity [13,14] due to the interaction between APB and dislocations has been reported in ordered Fe_3Al single crystals [7,9]. The temperature range for superelasticity in Fe_3Al alloys is approximately 250 K (from −50 °C to 200 °C), broader than that observed in superelasticity originating from the martensitic transformation which is typically 50 K [13]. Furthermore, the range of recovery strain is as high as 5 % and it makes Fe_3Al a potential shock-absorbing material. It should be noted that the superelasticity in Fe_3Al is strongly influenced by the density and distribution of APBs, i.e. the size and shape of APDs [7,9,15], as well as the aluminum concentration [16,17] (see Fig. 1). To date, considerable research has been conducted on the growth kinetics of APD in Fe_3Al alloys [18–33]. However, there is a significant difference between the mobility for $D0_3$-type ordering in Fe_3Al determined by Oki et al. [18] using X-ray diffraction (XRD) and that evaluated from the data of in-situ transmission electron microscopy (TEM) observation by Park [19].

Conversely, phase-field (PF) simulation [22–25] has been proven a powerful tool in investigating the migration of APBs and the kinetics of

* Corresponding authors.
E-mail addresses: okugawa@mat.eng.osaka-u.ac.jp (M. Okugawa), ykoizumi@mat.eng.osaka-u.ac.jp (Y. Koizumi).

https://doi.org/10.1016/j.actamat.2024.119958
Received 29 December 2023; Received in revised form 21 April 2024; Accepted 24 April 2024
Available online 25 April 2024

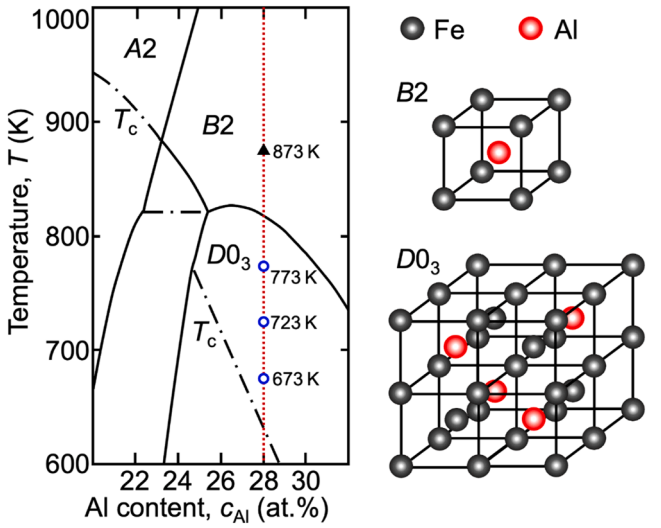

Fig. 1. Fe–Al phase diagram in the vicinity of 25 at.% Al [17]. The filled triangles represent the disorder annealing temperatures, while the open circles indicate the order annealing temperatures for Fe-28 at.% Al bulk alloys. Also, the unit cells of the ordered Fe–Al intermetallic compounds with *B*2 and $D0_3$ structures are shown.

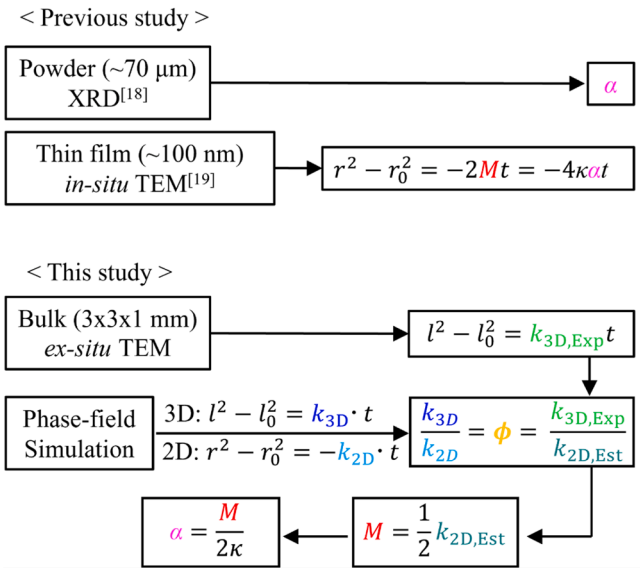

Fig. 2. Flowchart for determining the boundary mobility and ordering mobility of $D0_3$-type structure in Fe_3Al in the present study and previous studies using X-ray powder diffraction [18] and in-situ heating TEM observation [19].

microstructure evolution, especially in the initial stages of the developing process of ordered structure, which are very challenging to address experimentally. There have been reports on studies of the ordering kinetics in Fe_3Al alloys using PF simulations [26–33]. However, the ordering mobility for developing $D0_3$-structured Fe_3Al, or the growth kinetics for $D0_3$-type APD, which is indispensable for PF simulation, has not been investigated comprehensively. Therefore, in the present study, we tackle the issue of determining the ordering mobilities of the $D0_3$-type ordered structure in Fe_3Al by the combination of PF simulations and experimental observations. Moreover, the validity of this approach is confirmed by comparing the obtained ordering mobilities with literature data, and the results are discussed in the context of the effects of excess vacancy concentration, which is dependent on the thermal history.

2. Method

The methods used to determine the ordering mobility for the development of the $D0_3$-ordered structure in this study are illustrated in the flowchart presented in Fig. 2. Initially, the evolution kinetics of APD size following ex-situ aging using bulk samples is assessed through TEM observation. Subsequently, PF simulations are employed to imitate the process of circular APB shrinking in 2-dimensional (2D) space and APD growth in 3-dimensional (3D) space. These simulations provide the basis for estimating the shape coefficient governing the development of the $D0_3$-type ordering structure between the 2D and 3D models. Finally, by combining the experimental APD growth rate data with the shape coefficient determined through PF simulation, it becomes possible to evaluate the mobilities for $D0_3$-type APB migration and APD growth. The specific research methods are elaborated as follows:

2.1. Experimental procedure

In the present study, our initial focus was on investigating the evolution kinetics of the $D0_3$-type APD size in Fe_3Al through ex-situ heat treatment and TEM observation using bulk samples. As illustrated in Fig. 1, the Fe–Al binary phase diagram reveals the extensive formation of the BCC-based disordered *A*2 phase, as well as the ordered *B*2 and $D0_3$ phases in the vicinity of 25 at.% Al. Alloy with the concentration of 28 at.% Al was chosen for our study because it consistently resides in single-phase regions during temperature fluctuations, as depicted in Fig. 1. The preparation of bulk samples involved arc melting of pure elements, followed by annealing at 1523 K for 3.6×10^3 s for homogenization. Subsequently, small pieces measuring $3 \times 3 \times 1$ mm were cut for heat treatment. Disordering heat treatment was carried out at 873 K for 3.6×10^3 s, and ordering annealing was performed at 673 K, 723 K, and 773 K, followed by quenching in iced water. It is worth noting that the temperature for the disordering heat treatment falls within the *B*2-ordered phase region, yet it is referred to as disordering heat treatment in the present study, as our primary focus is to investigate the ordering mobility of the $D0_3$-ordered structure. Additionally, to mitigate the influence of *B*2-type APBs, the samples were annealed at 1073 K for 3.6×10^3 s before the disorder annealing at 873 K. Following the ordering annealing, the bulk samples were ground using dry emery paper and subjected to electro-polishing at −25 °C and 5 V. The APD size of the bulk samples annealed at various temperatures for various durations was subsequently measured via TEM, utilizing an acceleration voltage of 200 kV. According to Smoluchowski [34], Cupschalk [35], and Allen [36], the relationship between the APD size in 3D space and annealing time conforms to the parabolic law represented by the following equation:

$$l^2 - l_0^2 = k_{3D,Exp}t \tag{1}$$

where l and l_0 are the APD size at annealing time t and the initial state, respectively; and $k_{3D,Exp}$ is the kinetic coefficient determined from the experimental results.

2.2. Phase-field model

Although TEM observation allows us to determine the evolution kinetics of $D0_3$-APD size in 3D space, it is not feasible to directly derive the mobility of APBs migration in a 2D context or the mobility for $D0_3$-type ordered structure development in 3D space from experimental observation. This limitation arises because the curvature of APBs in bulk samples varies with annealing time. To address this challenge, our study introduces a novel approach for evaluating ordering mobility through the integration of PF simulation and experimental observation. More specifically, the shape coefficient, which characterizes the influence of APD shape on APD growth rate, and establishes the connection between the APD growth rate and APB migration rate for a given driving force, is

derived through PF simulations. Subsequently, by combining the shape coefficient with the experimentally determined 3D APD growth data using bulk samples, we can assess the mobilities for $D0_3$-type boundary migration and the development of $D0_3$-type ordering structures in the Fe_3Al.

The PF simulation methods used in the present study have been documented in previous studies [31,32,37,38]. Koizumi et al. [31–33] investigated the migration mobilities of $B2$- and $D0_3$-type APBs in nearly stoichiometric Fe_3Al at constant temperatures using the PF simulation and predicted the segregation of Fe atoms into the APBs, which was later confirmed experimentally by Murakami et al. [10] through transmission electron microscopy-electron energy loss spectroscopy (TEM-EELS) measurements. However, in these simulations, the values for the ordering energy were calculated using a constant derived from the stoichiometric composition, neglecting the concentration dependence of the gradient energy coefficient for simplicity in Koizumi et al.'s study [32]. In the present study, a PF model considering the concentration dependence of the gradient energy coefficient for $D0_3$-type APB migration and APD growth in Fe_3Al has been developed. The overall free energy of the system G_{sys}, which encompasses the gradient energy, is expressed as:

$$G_{sys} = \int \left\{ f\left(c_{Al}, c_v, \eta_{B2}, \eta_{D0_3}\right) + \kappa_{Al}(\nabla c_{Al})^2 + \kappa_{B2}(\nabla \eta_{B2})^2 + \kappa_{D0_3}\left(\nabla \eta_{D0_3}\right)^2 \right\} dV, \tag{2}$$

where f is the chemical Gibbs free energy, c_{Al} and c_v are the concentration of Al and vacancy, η_{B2} and η_{D0_3} are long-range order parameters of the $B2$ and $D0_3$ structures. κ_{Al}, κ_{B2}, and κ_{D0_3} are the gradient energy coefficients of the Al concentration, $B2$-type order parameter, and $D0_3$-type order parameter, respectively.

Considering there are four kinds of atom occupation sites in the $D0_3$-ordered structure [31,32], four sublattices were used to describe the structure of the $D0_3$-ordered phase. The long-range order parameter of the $B2$ structure is defined as:

$$\eta_{B2} = \left(\frac{y^{\alpha}_{Al} + y^{\beta}_{Al}}{2} - \frac{y^{\gamma}_{Al} + y^{\delta}_{Al}}{2} \right) \Big/ 2 \equiv \eta_1, \tag{3}$$

where y^{s}_{Al} $(s = \alpha, \beta, \gamma, \delta)$ represents the occupation probabilities of Al atoms on each sublattice. When $\eta_{B2} > 0$, the long-range order parameter of the $D0_3$ structure can be defined as:

$$\eta_{D0_3} = \frac{y^{\alpha}_{Al} - y^{\beta}_{Al}}{2} \equiv \eta_{2p}; \tag{4-1}$$

when $\eta_{B2} < 0$, the long-range order parameter of the $D0_3$ structure can be defined as:

$$\eta_{D0_3} = \frac{y^{\gamma}_{Al} - y^{\delta}_{Al}}{2} \equiv \eta_{2n}\ . \tag{4-2}$$

The atomic fraction of Al x_{Al} can be given by

$$x_{Al} = \frac{1}{4}\left(y^{\alpha}_{Al} + y^{\beta}_{Al} + y^{\gamma}_{Al} + y^{\delta}_{Al}\right). \tag{5}$$

By combing Eqs. (3)–(5), the occupation probabilities of Al atoms on each sublattice y^{s}_{Al} can be calculated using the atomic fraction of Al atoms and long-range order parameters of $B2$ and $D0_3$ structures.

The Bragg–Williams approximation [19], which can elucidate the relationship between free energy, degree of order, and solute concentration easily, is utilized to calculate the free energy of the system with the expression of

$$\Delta F = \frac{N_0}{2}\left\{ V(0)x_{Al}(1-x_{Al}) + V\left(\vec{k}_1\right)\eta^2_{B2} + V\left(\vec{k}_2\right)\eta^2_{D0_3} \right\} + k_B T \sum_{s=\alpha,\beta,\gamma,\delta} \left\{ y^{s}_{Al}\ln y^{s}_{Al} + \left(1-y^{s}_{Al}\right)\ln\left(1-y^{s}_{Al}\right) \right\} \tag{6}$$

where N_0 is the number of atoms in the system and k_B is Boltzmann constant; $V(\vec{k}_i)$ are the Fourier transforms of real space pair-interaction energies, $v(\vec{r})$, and are given by:

$$V\left(\vec{k}_i\right) = \sum_{\vec{r}} v(\vec{r}) \exp\left(-i\vec{k}_i \cdot \vec{r} \right) \tag{7}$$

where $\vec{k}_i$ is a reciprocal lattice vector and $v(\vec{r})$ is defined by:

$$v(\vec{r}) = \varepsilon^{r}_{FeFe} + \varepsilon^{r}_{AlAl} - 2\varepsilon^{r}_{FeAl} \tag{8}$$

where ε^{r}_{FeFe}, ε^{r}_{AlAl}, and ε^{r}_{FeAl} are bonding energies of Fe–Fe, Al–Al, and Fe–Al bonds of distance r, respectively. The values of $V(\vec{k}_i)$ used for simulations are the same as those determined by Park [19] considering the composition dependence. The first, second, and third nearest neighbor interaction energies v_1, v_2, and v_3 are calculated from $V(\vec{k}_i)$, and are expressed as follows and summarized in Supplemental Table S1 and Fig. S1:

$$\frac{v_1}{k_B} = 19070c_{Al}{}^3 - 23467c_{Al}{}^2 + 9423.8c_{Al} - 480.62 \tag{9-1}$$

$$\frac{v_2}{k_B} = -80870c_{Al}{}^3 + 68900c_{Al}{}^2 - 20242c_{Al} + 2305.8 \tag{9-2}$$

$$\frac{v_3}{k_B} = 25285c_{Al}{}^3 - 16767c_{Al}{}^2 + 3279c_{Al} - 298.74 \tag{9-3}$$

Hence, the gradient energy coefficients used in the present study in Eq. (2) are calculated using the concentration-dependent interaction energies v_1, v_2, v_3, and the separation between adjacent atomic planes Δx as shown in Eq. (10), which are the same as those derived by Park [19].

$$\kappa_{Al} = \frac{N_0}{2}\left(-v_1 - v_2 - 4v_3 \right)\Delta x^2 \tag{10-1}$$

$$\kappa_{B2} = \frac{N_0}{2}\left(v_1 - v_2 - 4v_3 \right)\Delta x^2 \tag{10-2}$$

$$\kappa_{D0_3} = \frac{N_o}{2}\left(\frac{1}{2}v_2 - 2v_3 \right)\Delta x^2 \tag{10-3}$$

The time evolution of the conservative order parameter $c_i(\boldsymbol{p}, t)$ (i =Al or Va (vacancy)) was obtained by solving the Cahn–Hilliard equation [37]:

$$\frac{\partial c_i(\boldsymbol{p}, t)}{\partial t} = \nabla \cdot \left[\sum_j \beta_{ij} \nabla \frac{\delta G_{sys}}{\delta c_i(\boldsymbol{p}, t)} \right], \tag{11}$$

where $\boldsymbol{p}$ is the vector of the position and β_{ij} is the mobility of the solute [39]. As per Koizumi et al. [32,40], the assessed boundary mobility obtained through PF simulation considering solute segregation is significantly lower than the intrinsic boundary mobility, which is primarily due to the solute drag effect of Al atoms. In light of this, to investigate the ideal boundary mobility of $D0_3$-type APB without the influence of solute drag effect resulting from solute segregation, β_{Al} is

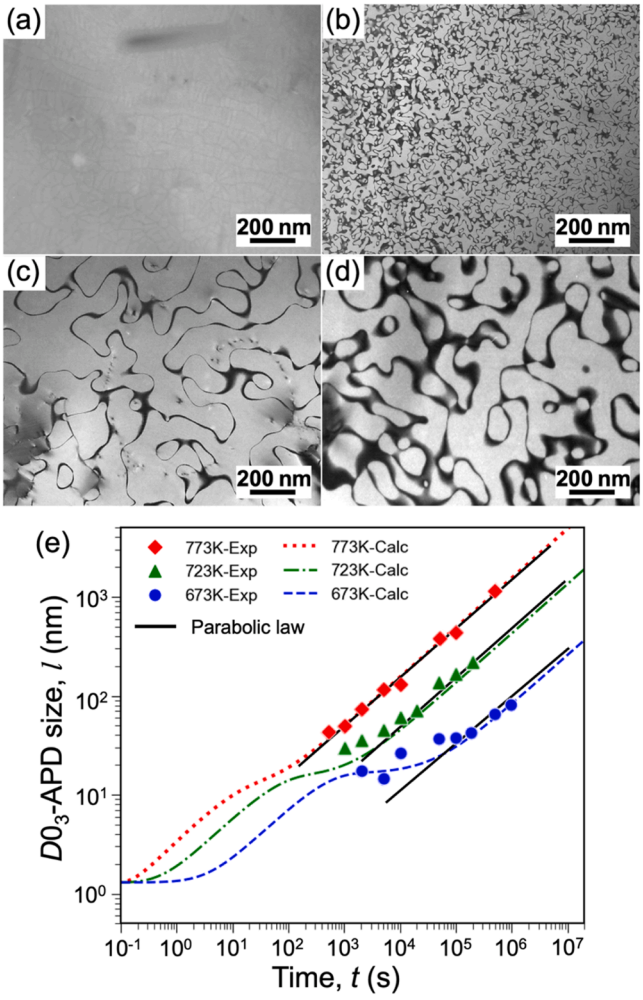

Fig. 3. (a–d) Darkfield images of Fe-28 at.% Al alloys quenched from 873 K and annealed at various temperatures for different periods: (a) as quenched, (b) 673 K for 2×10^3 s, (c) 673 K for 1×10^5 s, and (d) 723 K for 1×10^5 s. All images are captured with {111} superlattice reflection. (e) Average $D0_3$-type APD size as functions of annealing time determined using the bulk samples and the parabolic law fitted after the experimental results, as well as the calculated APD size considering variation of dynamic coefficient.

assumed to be 0 in the simulation to assess the correlation between the 3D APD growth rate and the 2D APB migration mobility.

Conversely, the time evolution of the non-conservative order parameter $\eta_i(\boldsymbol{p},t)$ ($i = B2$ or $D0_3$) was obtained by solving the Allen–Cahn equation [38,41]:

$$\frac{\partial \eta_i(\boldsymbol{p},t)}{\partial t} = -\sum_j \alpha_{ij} \frac{\delta G_{\mathrm{sys}}}{\delta \eta_i(\boldsymbol{p},t)}, \tag{12}$$

where α_{ij} is the ordering mobility. In the present study, the value of α_{ij} is taken from the evaluated results after Koizumi et al. [32] based on the experimental results of Oki [18].

The influence of vacancy concentration was also considered in this study. Therefore, the time evolutions of the conservative and non-conservative order parameters in Eqs. (11) and (12) are changed into the following expressions considering the solute mobility β_{Al} and ordering mobilities α_i as a function of vacancy concentration c_{v}, that is, $\beta_{\mathrm{Al}}(c_{\mathrm{v}})$ and $\alpha_i(c_{\mathrm{v}})$:

$$\frac{\partial c_{\mathrm{Al}}(\boldsymbol{p},t)}{\partial t} = \nabla\cdot\left\{\beta_{\mathrm{Al}}(c_{\mathrm{v}})\nabla\frac{\delta G_{\mathrm{sys}}}{\delta c_{\mathrm{Al}}}\right\} = \beta_{\mathrm{Al}}(c_{\mathrm{v}})\nabla^2\left(\frac{\delta G_{\mathrm{sys}}}{\delta c_{\mathrm{Al}}}\right) + \nabla\beta_{\mathrm{Al}}(c_{\mathrm{v}})\cdot\nabla\frac{\delta G_{\mathrm{sys}}}{\delta c_{\mathrm{Al}}}, \tag{13}$$

$$\frac{\partial \eta_i(\boldsymbol{p},t)}{\partial t} = -\alpha_i(c_{\mathrm{v}})\frac{\delta G_{\mathrm{sys}}}{\delta \eta_i(\boldsymbol{p},t)}\ . \tag{14}$$

Using Eqs. (2)–(14) to describe free energies and time evolution, we conducted 2D-PF simulations to replicate the shrinking of circular APBs and 3D-PF simulations to model the APD growth originating from the disordered state in Fe-28 at.% Al alloys. The annealing conditions for these PF simulations correspond to those employed in the experimental study.

2.3. Simulation conditions

The simulation box in the 2D-PF model is a square with a side length of 15 nm and is divided into a grid of 128×128 cells. Plane symmetry serves as the boundary condition for the PF simulation. Initially, a quarter-circle APB with a radius of 10 nm is established as the initial condition. This APB represents the $D0_3$-type APB in equilibrium at each annealing temperature. When the circular APB vanishes in the 2D simulation, the migration velocity V of the APB is calculated using Eq. (15) [32,38], where r signifies the APB radius at time t, and M denotes the boundary migration mobility. By taking r_0 as the initial radius, Eq. (16) can be derived from Eq. (15). This reveals that the relationship between the APD radius and annealing time adheres to a parabolic law.

$$V = \left|-\frac{\mathrm{d}r}{\mathrm{d}t}\right| = \frac{M}{r}, \tag{15}$$

$$r^2 - r_0^2 = -2Mt. \tag{16}$$

By treating $2M$ as $k_{2\mathrm{D}}$, Eq. (16) can be transformed into the following equation.

$$r^2 - r_0^2 = -k_{2\mathrm{D}}t. \tag{17}$$

In the case of the 3D-PF model, the simulation box takes the form of a cube with a side length of 15 nm, containing a grid with dimensions of $64 \times 64 \times 64$. Periodic boundary conditions are applied as the boundary conditions. The initial condition entails a $B2$-type order structure that is in equilibrium at each temperature. Subsequently, a minor perturbation is introduced in the $D0_3$-type order parameter. In the context of the 3D simulation, the relationship between APD size and annealing time also conforms to the parabolic law, as follows:

$$l^2 - l_0^2 = k_{3\mathrm{D}}t. \tag{18}$$

3. Results

Fig. 3a–d display dark-field images of the Fe-28 at.% Al alloys annealed at 673 and 723 K for varying durations after quenching from 873 K. All images were captured using {111} superlattice reflections. In

Table 1
Experimental determined kinetic coefficients and mobilities evaluated using shape coefficients determined by phase-field simulations.

Temperature [K]	$k_{3\mathrm{D,Exp}}$ [m^2/s]	$k_{2\mathrm{D,Est}}$ [m^2/s]	Boundary mobility, M [m^2/s]	Order mobility of $D0_3$, α_{D0_3} [m^3/(J s)]
673	9.20×10^{-21}	1.11×10^{-21}	5.54×10^{-22}	1.41×10^{-11}
723	3.10×10^{-19}	3.76×10^{-20}	1.88×10^{-20}	4.78×10^{-10}
773	2.27×10^{-18}	2.98×10^{-19}	1.49×10^{-19}	3.79×10^{-9}

Fig. 3a, there is no distinct APB visible in the as-quenched samples. However, upon annealing at 673 K for 2×10^3 s, as illustrated in Fig. 3b, APBs emerge as black lines in the dark-field image. With increased annealing time, the APB density decreases, resulting in APD growth, as seen in Fig. 3c. When the sample is annealed at a higher temperature for the same duration, a larger APD size is observed, as depicted in Fig. 3d.

The size of $D0_3$-type APD in bulk Fe-28 at.% Al alloys after aging are determined using linear intercepts through TEM observation, and the average results evaluated over varying annealing time are plotted in Fig. 3e. The kinetic coefficients for APD growth, denoted as $k_{3D,Exp}$, at different temperatures are derived by fitting these experimental data using the parabolic law in Eq. (1), with the results summarized in Table 1. As expected, the APD growth rate is higher at elevated temperatures. However, it is worth noting that the APD growth rate at the initial stage of 673 K exhibits a relatively substantial value and does not fully conform to the parabolic law. The cause of this deviation is believed to be due to the acceleration effect of the excess atomic vacancies introduced during the quenching process.

The parabolic law of APD growth, which is expressed by Eqs. (1) and (18), is derived from the following equation with assumptions that the growth rate (dl/dt) is proportional to the inverse of the APD size l and the coefficient k (i.e., $k_{3D,Exp}$ in Eq. (1), and k_{3D} in Eq. (18)) is constant (i.e. independent of annealing time t) with the initial APD size of l_0,

$$\frac{dl}{dt} = \frac{k}{2l} \ . \tag{19}$$

However, the coefficient k can vary with time when the vacancy concentration varies with time. As pointed out by Sakai and Mikkola [42], the growth of APD is diffusion-controlled process. Diffusion for APD growth is considered to be caused by vacancy mechanism, and the diffusivity by single vacancy mechanism is proportional to vacancy concentration. This is because the migration of APB is caused by the migration of constituent atoms which shifts the "phase" of ordered arrangement of two different atom species by exchanging their mutual location via vacancy. Therefore, Eq. (19) can be transformed into the following equation:

$$\frac{dl}{dt} = \frac{k_0 c_v}{2l} = \frac{\mu_0 c_v}{2l} D_0 P_m \gamma(t). \tag{20}$$

where k_0 and μ_0 are constants, D_0 is frequency factor, and c_v is vacancy concentration. P_m is the jump probability of vacancy and γ is APB energy.

The equilibrium vacancy concentration at temperature T in the general bulk samples can be calculated using the following equation:

$$c_v^{eq}(T) = c_0 \exp\left(-\frac{Q_f}{RT}\right), \tag{21}$$

where Q_f is the formation energy of vacancy, R is gas constant. After disordering annealing, the samples are quenched and then annealed at a lower temperature for ordering. The time evolution of the vacancy concentration in the samples during ordering annealing is calculated using the following equation:

$$\begin{aligned} c_v(t) &= c_{v,a}^{eq} + \left(c_{v,q}^{eq} - c_{v,a}^{eq}\right)\exp\left(-\frac{t}{\tau_v}\right) \\ &= c_0\left\{\exp\left(-\frac{H_f}{RT_a}\right) + \left[\frac{c_0^{B2}}{c_0}\exp\left(-\frac{H_f^q}{RT_q}\right) - \exp\left(-\frac{H_f}{RT_a}\right)\right]\right\}\exp\left(-\frac{t}{\tau_v}\right), \end{aligned} \tag{22}$$

where $c_v(t)$ is the vacancy concentration at time t. $c_{v,q}^{eq}$ and $c_{v,a}^{eq}$ are equilibrium vacancy concentrations at the quenching temperature and ordering annealing temperature, respectively. H_f and H_f^q are the formation enthalpy of vacancy at annealing temperature and quenching temperature, respectively. τ_v is the relaxation time for the excess vacancies to disappear, which is given by:

$$\tau_v = \tau_{0v}\exp\left(\frac{Q_v}{RT}\right), \tag{23}$$

On the other hand, the jump probability of vacancy P_m is calculated by:

$$P_m = \exp\left(-\frac{H_m}{RT}\right), \tag{24}$$

where H_m is the enthalpy of vacancy migration. The experimental data used for calculation are available in the literature [43–47] and are summarized in Table S2 in the supplemental materials.

In contrast, the time variation of APB energy during annealing is also evaluated. The APB energy and the LRO hold the following relationship:

$$\gamma(t) = \gamma_0 \eta(t)^2, \tag{25}$$

where γ_0 is constant, and η during annealing can be expressed as:

$$\frac{d\eta}{dt} = \frac{1}{\tau_s}\left(\eta_{eq} - \eta\right)^3, \tag{26}$$

where η_{eq} is the equilibrated LRO at each annealing temperature, and τ_s is the relaxation time for ordering. τ_s in Eq. (26) hold the Arrhenius relationship as shown in the following equation:

$$\tau_s = \tau_{0s}\exp\left(\frac{Q_s}{RT}\right), \tag{27}$$

where τ_{0s} and Q_s are a time constant and the activation energy for the developlment of LRO (i.e. ordering), respectively. The parameters are used as fitting parameters to reproduce the experimentally measured change in the APD growth qualitativiely in this study.

By combining Eqs. (21)–(27), the evolution of APD size along with the annealing time is calculated using Eq. (20) and is plotted in Fig. 3e for comparison. It is noteworthy that the calculated APD size increases rapidly at the initial stage of annealing. Then the growth rates exhibit a relatively steady flat stage, followed by a constant growth rate which conforms to the parabolic law. As mentioned previously, the experimentally determined APD sizes at the initial stage of annealing is relatively large values and deviate from the parabolic law. However, as can be seen in Fig. 3e, the calculated APD size agrees well with the experimentally measured data, confirming the promotion effect of the excess atomic vacancy on the APD growth during the initial stage of annealing.

Fig. 4 presents the simulated results of 2D circular APB shrinking (Fig. 4a1–a4) and 3D APD growth (Fig. 4b1–b4) after annealing at 673 K, by way of example. In the 2D simulation result, which is colored by the degree of the $D0_3$ order parameter in Fig. 4a1–a4, the APB is identifiable as the black diffuse interface between the blue quarter-circle area where $\eta_{D03} < 0$ and the surrounding red area where $\eta_{D03} > 0$. The APD shrinks with annealing time, and the boundary migration mobility can be determined from the relationship involving the rate of APB migration, as previously mentioned. Conversely, in the 3D simulation results (Fig. 4b1–b4), the $D0_3$-type APBs are visualized as a red iso-surface of $\eta_{D03} > 0$. In the 3D APD growth simulation, the APBs display irregular curvatures across the entire simulation box. With increasing annealing time, the density of APBs decreases, leading to an increase in APD size. Linear intercepts of APB (l) are calculated as a measure of APD size and plotted against annealing time, as shown in Fig. 4d. The simulation results for 3D APD growth are in agreement with the experimental results depicted in Fig. 3. The radius of $D0_3$-APB and size of $D0_3$-APD, as functions of annealing time, are presented in Fig. 4c and d, respectively. According to the simulation results, the kinetic coefficients in the 2D and 3D PF simulations, denoted as k_{2D} and k_{3D}, were evaluated using line fitting with the parabolic law outlined in Eqs. (17) and (18). The values of the obtained kinetic coefficients for each annealing temperature are listed in Table 2.

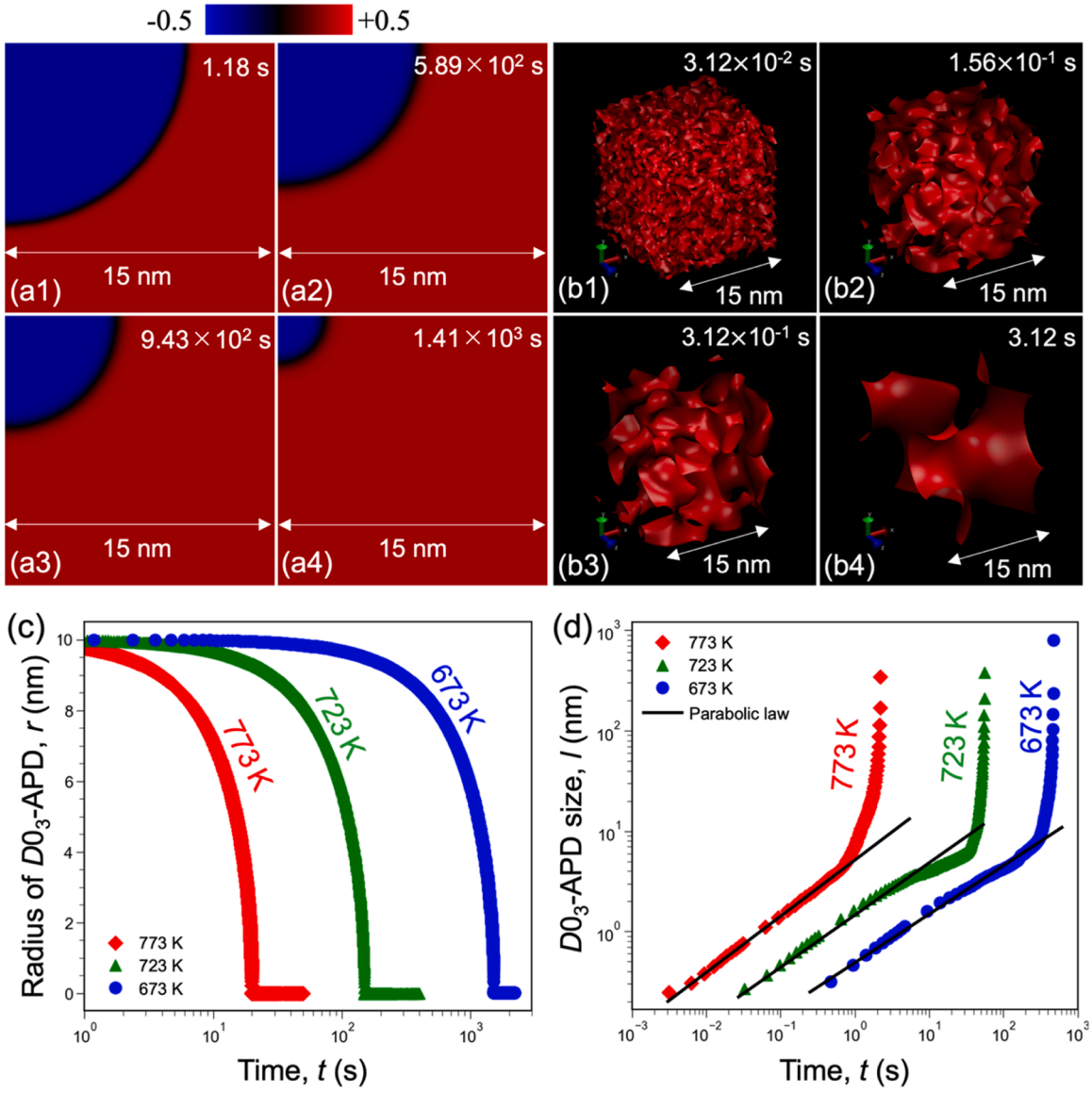

Fig. 4. Phase-field simulation results of Fe-28 at.% Al alloy quenched from 873 K: (a1–a4) snapshots of 2D shrinking circular $D0_3$-APBs at 673 K for 1.18 s, 5.89 × 10^2 s, 9.43 × 10^2 s, and 1.41 × 10^3 s, respectively. (b1–b4) snapshots of 3D $D0_3$-APD growth at 673 K for 3.12 × 10^{-2} s, 1.56 × 10^{-1} s, 3.12 × 10^{-1} s, and 3.12 s, respectively. (c) APB radius in the 2D PF simulations and (d) average APD size in the 3D PF simulations changing with annealing time at different temperatures.

Table 2
Kinetic coefficients and shape coefficients evaluated by phase-field simulations.

Temperature [K]	k_{2D} [m^2/s]	k_{3D} [m^2/s]	Shape coefficient, ϕ (= k_{3D}/k_{2D})
673	6.63 × 10^{-20}	5.50 × 10^{-19}	8.30
723	6.69 × 10^{-19}	5.51 × 10^{-18}	8.23
773	5.01 × 10^{-18}	3.82 × 10^{-17}	7.62

According to Allen and Cahn [38], the time evolution of APD size during coarsening can be expressed by the following equation with the assumption that the general morphological features of the APD remain unchanged:

$$[S_v(t)]^{-2} - [S_v(0)]^{-2} = 2\phi Mt \tag{28}$$

where $S_v(t)$ and $S_v(0)$ are the surface area in a unit volume of specimen at time t and at the initial state, respectively; and S_v is related to the mean linear intercept l by $S_v = 2/l$.

In Eq. (28), ϕ is a geometrical factor given by:

$$K_m^2 = \phi S_v^2 \tag{29}$$

where K_m^2 is the averaged square mean curvature of the APBs [38] defined by

$$K_m^2 = \langle (K_1 + K_2)^2 \rangle = \frac{1}{S}\int (K_1 + K_2)^2 dS \tag{30}$$

where S is the experimentally measurable total surface area of the specimen. K_1 and K_2 are the principal curvatures of the isosurfaces of the APBs. However, the values of ϕ have not yet been determined theoret-

ically or experimentally due to the complexity of the curvatures of the three-dimensional APBs.

In the present study, the influence of APD morphology on APB migration mobility is examined based on the 2D- and 3D-PF simulation results. The shape coefficient ϕ, with the same conceptual basis as the geometrical factor in Eq. (28), is suggested to correspond to the ratio between the coefficients of the parabolic law in 3D APD growth from the disordered state and those in 2D circular APB shrinking. Specifically, the shape coefficient ϕ is calculated using the kinetic coefficients derived from the 2D- and 3D- PF simulations as presented in Eqs. (17) and (18), thus, k_{3D}/k_{2D}. The values of the shape coefficient are also documented in Table 2. They are all around 8 and remain nearly identical across all three temperatures examined. As anticipated, this finding aligns with expectations dating back to 1979 by Allen and Cahn [38], demonstrating its temperature independence and establishing an approximate value of 8. This determined value provides a basis for further analysis.

Assuming that the shape coefficient holds consistent between the experiment and PF simulation, and with the aid of the experimentally determined $k_{3D,Exp}$, it becomes possible to estimate the kinetic coefficient of 2D APB migration $k_{2D,Est}$. This estimation, which is particularly challenging to ascertain experimentally, can be calculated using the following equation:

$$\phi = \frac{k_{3D}}{k_{2D}} = \frac{k_{3D,Exp}}{k_{2D,Est}} \ . \tag{31}$$

The experimental boundary mobility M can then be obtained using the following equation:

$$M = \frac{1}{2} k_{2D,Est} \ . \tag{32}$$

Moreover, Allen and Cahn [38] indicated that the ordering mobility α and boundary mobility M have the following relationship when using the gradient energy coefficient κ:

$$\alpha = \frac{M}{2\kappa} \ . \tag{33}$$

The value of κ is evaluated as 1.97×10^{-11} J/m, according to the Bragg–Williams approximation [32], and then, the ordering mobility for the developing of $D0_3$-ordered structure, α_{D0_3}, can be derived. The evaluated values of $k_{2D,Est}$, M, and α_{D0_3} using Eqs. (31)–(33) are listed in Table 1.

The obtained mobilities of boundary migration and $D0_3$-type ordering in this study are presented in Fig. 5a and b, respectively. Additionally, the previously reported mobilities, as assessed through the kinetics of powder XRD analysis [18] and thin-film in-situ heating TEM observations [19], are included in Fig. 5 for comparison. As depicted in Fig. 5, the results obtained in the present study closely approximate those derived from powder XRD. However, the results from thin-film TEM observations indicate a significantly higher value. Specifically, the ordering mobility determined from TEM observations using thin film at 673 K ($\alpha_{TEM,\ 673K} = 8.18 \times 10^{-10}$ m^3/(J s)) is nearly 25 and 58 times higher than that calculated from the results of powder XRD ($\alpha_{XRD,\ 673K}$=3.27×10^{-11} m^3/(J s)) and the present study ($\alpha_{Present,\ 673K} = 1.41 \times 10^{-11}$ m^3/(J s)), respectively.

4. Discussion

4.1. Shape coefficient

Since the 1930s, a considerable volume of experimental research has been dedicated to exploring the ordering kinetics of intermetallic compounds using techniques such as X-ray diffraction (XRD), electrical resistivity measurement, and direct in-situ TEM observation [48–55]. However, the specimens utilized in these investigations have been powders or thin films. The investigation of ordering kinetics in bulk materials has remained elusive owing to the spatial and temporal variations in the curvatures of APBs during APD growth in 3D space. This complexity has made the determination of ordering mobility a formidable challenge. In the 1970s, the ordering kinetics of the development of a $D0_3$-type ordered structure in Fe_3Al were studied by Oki [18] using powder subjected to ordering heat treatment followed by XRD. Park [19] measured the kinetics by in-situ TEM observation in the 1980s. However, the consistency between the values of ordering kinetics obtained from these separate studies has never been examined. In the present study, the flow chart for determining the ordering mobilities in these two studies is also illustrated in Fig. 2. Oki et al. [18] explored the time-dependent changes in the degrees of order in $B2$- and $D0_3$-type ordered structures using XRD with Fe-26 at.% Al powders and calculated the ordering mobility based on experimental results. Conversely, Park [19] measured the radius of $D0_3$-type APB as it shrank using TEM in an in-situ heated Fe-26 at.% Al thin film. The APB migration mobility M was calculated using the same equation as described in Eq. (16), and

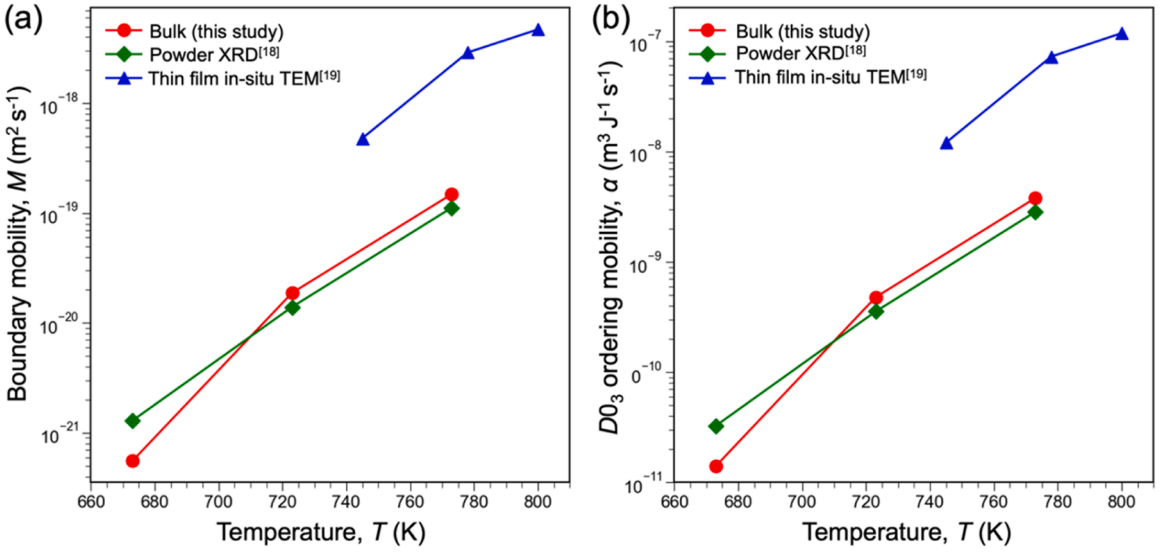

Fig. 5. Comparison of (a) boundary mobility of $D0_3$-APBs and (b) ordering mobility of $D0_3$-type structures in Fe_3Al evaluated using various methods, including powder X-ray diffraction and heat treatment [18], in-situ TEM observation of shrinking APD [19], and the combination of heat treatment of bulk samples and subsequent TEM observation associated with PF simulations (this study).

then the mobility of the $D0_3$-type ordering, denoted as α_{D0_3}, was evaluated using Eq. (33). However, the ordering mobilities obtained from these two studies exhibit significant differences, as evident in Fig. 5. Furthermore, the size and shape of the samples used in these two studies (powders and thin film) differ significantly from those intended for practical applications, potentially affecting the kinetics of relaxation of quenched lattice defects, particularly the excess atomic vacancies.

The growth kinetics of APDs in bulk intermetallic have long posed a challenge because of the variations in curvatures in 3D space. Allen and Cahn [38] have developed an APD coarsening equation relating the averages of curvature to APB migration velocity as shown in Eqs. (28)–(30), involving the geometrical factor ϕ and the averaged square mean curvature K_m^2. However, the values of ϕ have not been determined due to the complexity of the APB morphology in 3D space.

In the present study, the shape coefficient, serving as the link between boundary mobility in 2D and APD growth rate in 3D, is evaluated using the ratio between the coefficients of the parabolic law in 3D APD growth from the disordered state and those in 2D circular APB shrinking. Through the integration of PF simulations involving 2D circular APB shrinkage and 3D APD growth, the coefficients of the parabolic law (specifically k_{3D} and k_{2D}) were estimated. Subsequently, the shape coefficient was calculated using the ratio k_{3D}/k_{2D}, which demonstrates a temperature-independent value of approximately 8. Conversely, the kinetic coefficient of parabolic law in APD size evolution in bulk samples ($k_{3D,Exp}$) were determined experimentally. Based on the primary hypothesis that the shape coefficient is equivalent in the simulations and in the experiment, the boundary mobility and ordering mobility of $D0_3$-type ordered structure in bulk Fe_3Al can be evaluated using the shape coefficient obtained from PF simulations.

Based on the 3D-PF simulation results conducted by this study, the value of ϕ is also assessed using the original expression proposed by Allen and Cahn [38] in Eq. (29). S_v is calculated from the mean linear intercepts of the simulated $D0_3$ APD by $S_v = 2/l$, and the averaged square mean curvature K_m^2 is evaluated by analyzing the curvatures of the iso-surface of $D0_3$-type APBs in 3D PF simulations, e.g., the snapshots in Fig. 4b1–b4. The obtained shape coefficients using Eq. (29) are plotted in Fig. S2 as functions of the linear intercepts of the simulated $D0_3$ APD, which also demonstrate nearly identical values around 8 when the APD size is smaller than 5 nm (which consist with the range of APD size used for parabolic law fitting as denoted in Fig. 4d). When the APD size is larger than 5 nm, the values of the shape coefficient decrease abnormally and the reason is thought to be the deviations of the evaluated curvatures of the APBs due to the influences of the size of the simulation box. From these results, we can see that the shape coefficient in this study is the same as the geometrical factor introduced by Allen and Cahn [38]. Moreover, in this study, the shape coefficient is determined by comparing the coefficients of the parabolic law obtained from 3D and 2D PF simulations. Consequently, only the dynamic coefficients were utilized in the calculation to decrease inaccuracies in APD size and other potential influences.

4.2. Effect of specimen size

The ordering mobilities of $D0_3$-type structure in Fe_3Al, as evaluated by different research groups and presented in Fig. 5, exhibit significant disparities. The samples used in these experiments differ significantly in size and shape, which is considered to have a profound effect on the obtained ordering mobilities. In Oki's study [18], powders with diameters of approximately 70 μm were employed for order-order relaxation analysis using XRD. In this case, the ordering mobility was assessed by monitoring changes in the crystal structure. The size of powders is considered to be sufficiently large compared to the size of APDs (smaller than 1 μm) and the effect of size was considered to be negligible. Conversely, thin film with an average thickness of around 100 nm was used in the in-situ TEM observation of APB migration by Park [19]. It is widely recognized that atomic diffusion occurs more readily on the sample surface than in the bulk, owing to the reduced constraints from surrounding atoms on the sample surface in comparison to those inside the bulk [56]. The presence of defects near the sample surface increases the feasibility of atom diffusion, primarily through the vacancy mechanism [57–59]. The specific surface area of the film used in Park's experiment is significantly greater than that of bulk samples, which enhanced atom diffusion due to the thin-film effect [60,61], ultimately leading to the observed higher value of ordering mobility (as seen in Fig. 5).

In the present research, to gain insights into the ordering mobilities of $D0_3$-type structure in Fe_3Al intended for practical applications, plate-shaped bulk samples with dimensions of 3 × 3 × 1 mm were employed for ex-situ heat treatment and TEM observation. Additionally, PF simulations were conducted to estimate the shape coefficient for APD growth. By integrating the experimental data obtained from bulk samples with the calculated shape coefficient, the ordering mobilities of $D0_3$-type structure in Fe_3Al were determined. These findings align closely with the values evaluated through powder XRD by Oki et al. [18].

4.3. Role of atomic vacancies on ordering mobility

In addition to the effect of specimen size, the excess vacancies introduced by quenching are also believed to play a role in accounting for the discrepancy in ordering mobility. Fig. 6 provides a schematic illustration of the transfer of atoms and vacancies that accompany the migration of APB on the {110} plane in $D0_3$-ordered Fe_3Al. In the

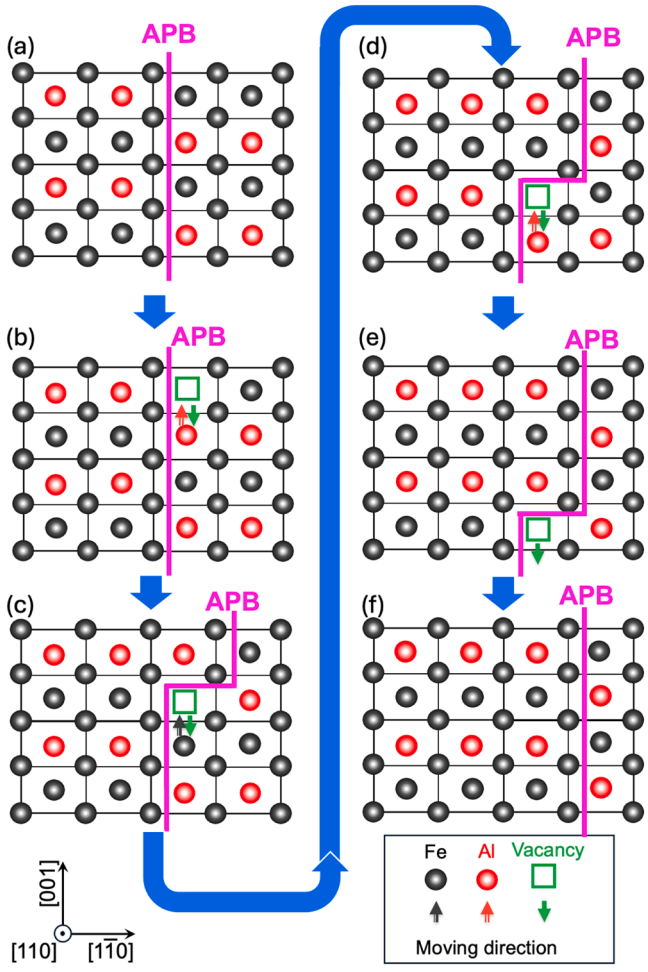

Fig. 6. Schematic illustrations showing the motions of atoms and vacancies during APB migration on {110} plane in Fe_3Al with $D0_3$-ordered structure.

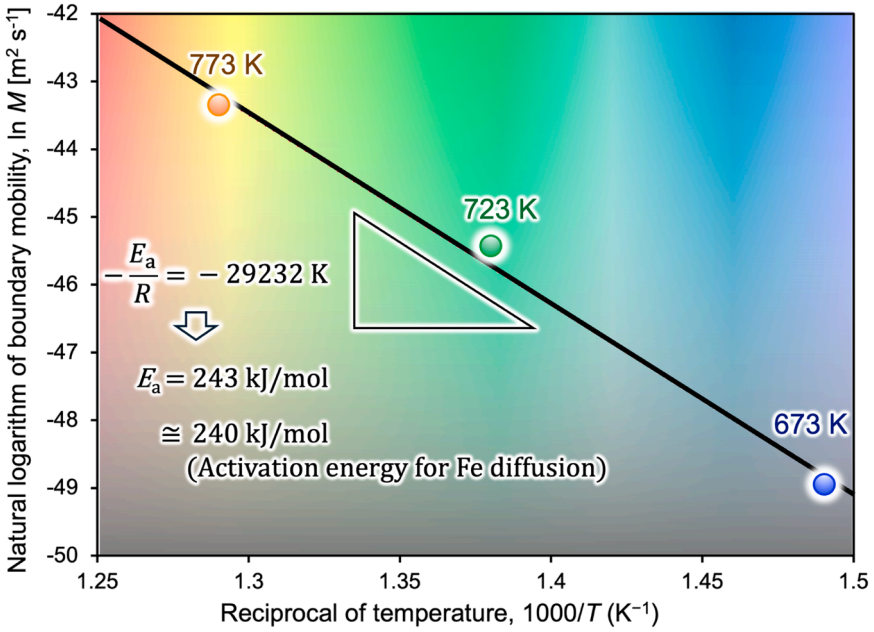

Fig. 7. Arrhenius plot of boundary mobility of $D0_3$-type APB in Fe_3Al evaluated from the experimental data of 3D APD growth in the bulk in the present study.

illustration, black and red balls represent Fe and Al atoms, respectively. The adjacent domains, separated by the APB, exhibit different atom arrangements. In the context of bulk diffusion of minority atoms in A_3B-type compounds, the formation of anti-site atoms is required [62]. However, this is not a necessity for the diffusion of Al atoms on the APB because anti-site atoms are already formed in proximity to the APB. Furthermore, the diffusion of both Al and Fe atoms near the APB can be facilitated by the presence of atomic vacancies, represented by green squares in Fig. 6. This figure illustrates that the APB moves by an interatomic distance due to the motion of vacancies and atoms on the right side of the APB, indicated by the vertical arrows. Consequently, the migration of the APB is driven by the movement of atoms along the APB through a vacancy mechanism, involving the exchange of sites between substitutional minor solute atoms (i.e., Al in Fe_3Al) and atomic vacancies. Therefore, a higher vacancy concentration is beneficial for APB migration.

The equilibrium vacancy concentration at temperature T in the general bulk samples can be calculated using Eq. (22). After disordering annealing, the samples are quenched and then annealed at a lower temperature for ordering. The vacancy concentration in the equilibrium state at the high disordering annealing temperature is maintained within the samples at the initial period of ordering annealing, resulting in the presence of excess vacancies. Therefore, samples quenched from a higher temperature, in this case, the thin film used in Park's [19] study, will have higher excess vacancy concentration, resulting in the promotion effect on the ordering kinetic, which is consistent with the results shown in Fig. 5.

Furthermore, the activation energy for the diffusion of Al atoms in the Fe_3Al alloys can be expressed as:

$$Q_{\mathrm{Diff}} = E_{\mathrm{F}}^{\mathrm{Al(Fe)}} + E_{\mathrm{F}}^{\mathrm{Va(Al)}} + E_{\mathrm{m}}, \tag{34}$$

where $E_{\mathrm{F}}^{\mathrm{Al(Fe)}}$ is the formation energy of the Al atom at the anti-site (the Fe site); $E_{\mathrm{F}}^{\mathrm{Va(Al)}}$ is the formation energy of vacancy at the Al site, and E_{m} is the migration energy of atoms. In the case of vacancy-induced diffusion, E_{m} is equivalent to the migration energy of vacancy.

In contrast, as mentioned previously, there is no need to form anti-site Al atoms in the migration of APB. Also, the Al-site and Fe-site cannot be distinguished. Subsequently, the activation energies for atom diffusion on APB can be expressed as:

$$Q_{\mathrm{APB}} = E_{\mathrm{F}}^{\mathrm{Va(Al)}} + E_{\mathrm{m}}, \tag{35}$$

which is smaller than the activation energy for Al diffusion in Fe_3Al bulk, and essentially the same as that for Fe diffusion. Therefore, atom diffusion is easier to occur on APB than inside of the bulk.

The experimentally determined formation energy ($E_{\mathrm{F}}^{\mathrm{Va}}$) and migration energy ($E_{\mathrm{m}}$) of vacancy in $D0_3$-structured Fe_3Al alloys are 1.18 eV and 1.31 eV [63], respectively. Therefore, the activation energy for the migration of $D0_3$-type APB in Fe_3Al alloys can be calculated to be 2.49 eV, i.e., 240.22 kJ/mol using Eq. (35). On the other hand, the Arrhenius equation can be expressed as follows:

$$k = A\exp\left(\frac{-E_a}{RT}\right), \tag{36}$$

where k is the rate constant, A is the Arrhenius factor, R is the universal gas constant, T is the absolute temperature, and E_a is the activation energy. Taking the natural logarithm of the Arrhenius equation, Eq. (36) can be translated to the next equation:

$$\ln k = \ln A - \frac{E_a}{R}\frac{1}{T}, \tag{37}$$

from which we can see that, the activation energy can be evaluated using the slope of Eq. (37). Hence, an Arrhenius plot for the migration mobility of $D0_3$-type APB using the boundary mobilities evaluated in the present study is shown in Fig. 7, and the dashed line represents the fit of the Arrhenius equation to the data points. Hence, the activation energy for $D0_3$-type APB migration is evaluated to be 242.92 kJ/mol, the value of which is very close to the experimental results obtained using Eq. (35).

In contrast to the abnormally high values obtained from thin-film in-situ TEM observations, the boundary and ordering mobilities based on powder XRD and those determined in the present study are more reliable [18]. Furthermore, the time evolution of APD structures in bulk samples holds greater practical significance. Therefore, the method for determining the boundary and ordering mobilities of APD through the combination of PF simulation and TEM observation using bulk samples, as demonstrated in the present study, has proven to be an efficient and dependable approach. Furthermore, the methodology developed in this study has the potential to be extended to other alloy systems such as

Heusler alloys with $L2_1$ structures [64,65], which also feature BCC-based ordered structures and are currently garnering substantial attention as materials for spintronics and shape memory alloys (e.g., Co_2MnAl and Ni_2MnGa).

5. Conclusions

The ordering mobilities of the $D0_3$-type structure in Fe_3Al were assessed by integrating experimental observations using bulk samples and phase-field simulations. The following conclusions can be drawn:

- Innovative integration of experimental and simulation methodologies has led to a significant advancement in understanding the ordering mobility of $D0_3$-type Fe_3Al structures. The quantification of the elusive shape coefficient validates the effectiveness of the combination of 2D- and 3D- phase field (PF) simulations.
- The shape coefficient plays a pivotal role in the precise correlation between boundary mobility and ordering mobilities, informed by APD growth kinetics, thereby overcoming traditional experimental limitations. Our results align with those from classical order-order relaxation experiments and X-ray diffraction (XRD) analyses of heat-treated powders, confirming our approach and providing new insights into APD growth and ordering kinetics.
- The synergy between PF simulations and experimental methods emerges as a powerful strategy for managing superelasticity influenced by the interaction between superdislocations and APD boundaries. Additionally, the resemblance of the $D0_3$- structure of Fe_3Al to the $L2_1$-structure opens new paths for exploring ordering mechanisms that are anticipated to improve the properties of Heusler alloys, which are essential in the realm of spintronics.

CRediT authorship contribution statement

Yuheng Liu: Conceptualization, Data curation, Funding acquisition, Investigation, Methodology, Project administration, Validation, Visualization, Writing – original draft, Writing – review & editing. **Madoka Watanabe:** Data curation, Formal analysis, Investigation, Methodology, Validation, Visualization, Writing – original draft. **Masayuki Okugawa:** Conceptualization, Data curation, Formal analysis, Investigation, Methodology, Software, Supervision, Validation, Visualization, Writing – original draft, Writing – review & editing. **Takashi Hagiwara:** Conceptualization, Data curation, Formal analysis, Investigation, Methodology, Project administration, Resources, Software, Supervision, Validation, Visualization, Writing – original draft, Writing – review & editing. **Tsubasa Sato:** Data curation, Investigation, Methodology, Resources, Validation, Visualization, Writing – original draft, Writing – review & editing. **Yusuke Seguchi:** Data curation, Investigation, Software. **Yoshitaka Adachi:** Data curation, Investigation, Software. **Yoritoshi Minamino:** Conceptualization, Supervision, Writing – review & editing. **Yuichiro Koizumi:** Conceptualization, Data curation, Formal analysis, Funding acquisition, Investigation, Methodology, Project administration, Resources, Software, Supervision, Validation, Visualization, Writing – original draft, Writing – review & editing.

Declaration of competing interest

The authors declare that they have no known competing financial interests or personal relationships that could have appeared to influence the work reported in this paper.

Acknowledgments

This work was supported by the Japan Society for the Promotion of Science (JSPS KAKENHI Grant nos. 21H05018, 21H05193, 23K13578, 21H05192, and 21H05194). We greatly appreciate Prof. Toshiyuki Koyama of Nagoya University for providing the program code on which the simulation of the present study is based. Also, this study was supported by the promotion program for internationalization of university in 2007 by MEXT, the Yamada Science Foundation Overseas Research Support in 2006, the 19th ISIJ Research Promation Grant. YK expresses gratitude to Prof. Samuel M. Allen (currently MIT emeritus) for the fruitful discussions at the onset of this research in 2007 and for providing data from W. Park's Ph. D thesis.

Supplementary materials

Supplementary material associated with this article can be found, in the online version, at doi:10.1016/j.actamat.2024.119958.

References

[1] J. Sato, T. Omori, K. Oikawa, I. Ohnuma, R. Kainuma, K. Ishida, Cobalt-base high-temperature alloys, Science 312 (5770) (2006) 90–91.
[2] R. Song, J. Han, M. Okugawa, R. Belosludov, T. Wada, J. Jiang, D. Wei, A. Kudo, Y. Tian, M. Chen, H. Kato, Ultrafine nanoporous intermetallic catalysts by high-temperature liquid metal dealloying for electrochemical hydrogen production, Nat. Commun. 13 (1) (2022) 5157.
[3] W.J. Zeng, C. Wang, Q.Q. Yan, P. Yin, L. Tong, H.W. Liang, Phase diagrams guide synthesis of highly ordered intermetallic electrocatalysts: separating alloying and ordering stages, Nat. Commun. 13 (1) (2022) 7654.
[4] R.Y. Umetsu, H. Ishikawa, K. Kobayashi, A. Fujita, K. Ishida, R. Kainuma, Effects of the antiferromagnetic anti-phase domain boundary on the magnetization processes in Ni_2Mn ($Ga_{0.5}Al_{0.5}$) Heusler alloy, Scr. Mater. 65 (1) (2011) 41–44.
[5] Y. Koizumi, Y. Minamino, T. Nakano, Y. Umakoshi, Effects of antiphase domains on dislocation motion in Ti_3Al single crystals deformed by prism slip, Philos. Mag. 88 (4) (2008) 465–488.
[6] W. Yuan, G. Niu, Y. Xian, H. Wu, H. Wang, H. Yin, P. Liu, W. Li, J. Fan, In situ regulating the order-disorder phase transition in $Cs_2AgBiBr_6$ single crystal toward the application in an X-ray detector, Adv. Funct. Mater. 29 (20) (2019) 1900234.
[7] H.Y. Yasuda, K. Nakano, T. Nakajima, M. Ueda, Y. Umakoshi, Effect of ordering process on giant pseudoelasticity in Fe_3Al single crystals, Acta Mater. 51 (17) (2003) 5101–5112.
[8] H.Y. Yasuda, M. Aoki, Y. Umakoshi, Effect of the ordering process on pseudoelasticity in Fe_3Ga single crystals, Acta Mater. 55 (7) (2007) 2407–2415.
[9] H.Y. Yasuda, T. Nakajima, K. Nakano, K. Yamaoka, M. Ueda, Y. Umakoshi, Effect of Al concentration on pseudoelasticity in Fe_3Al single crystals, Acta Mater. 53 (20) (2005) 5343–5351.
[10] Y. Murakami, K. Niitsu, T. Tanigaki, R. Kainuma, H.S. Park, D. Shindo, Magnetization amplified by structural disorder within nanometre-scale interface region, Nat. Commun. 5 (1) (2014) 1–8.
[11] Z. Nedelkoski, A.M. Sanchez, A. Ghasemi, K. Hamaya, R.F.L. Evans, G.R. Bell, A. Hirohata, V.K. Lazarov, The antiphase boundary in half-metallic Heusler alloy $Co_2Fe(Al, Si)$: atomic structure, spin polarization reversal, and domain wall effects, Appl. Phys. Lett. 109 (22) (2016) 222405.
[12] P.J. Maziasz, C.T. Liu, G.M. Goodwin, Overview of the Development of FeAl Intermetallic Alloys (No. CONF-950908-2), Oak Ridge National Lab. (ORNL), Oak Ridge, TN (United States), 1995.
[13] K. Otsuka, C.M. Wayman, Shape Memory Materials, Cambridge University Press, Cambridge, 1999.
[14] K. Otsuka, X. Ren, Recent developments in the research of shape memory alloys, Intermetallics 7 (5) (1999) 511–528.
[15] K. Yoshimi, H. Terashima, S. Hanada, Effect of APB type on tensile properties of Cr added Fe_3Al with $D0_3$ structure, J. Mater. Sci. Eng. A 194 (1) (1995) 53–61.
[16] A. Mulyawan, T. Terai, T. Fukuda, Interpretation of Fe-rich part of Fe–Al phase diagram from magnetic properties of $A2$-, $B2$-, and $D0_3$-phases, J. Alloys Compd. 834 (2020) 155140.
[17] O. Ikeda, I. Ohnuma, R. Kainuma, K. Ishida, Phase equilibria and stability of ordered BCC phases in the Fe-rich portion of the Fe–Al system, Intermetallics 9 (9) (2001) 755–761.
[18] K. Oki, J. Masuda, M. Hasaka, Kinetics of ordering in Fe_3Al alloys, Trans. JIM 39 (6) (1975) 589–595 (in Japanese).
[19] W. Park, Migration kinetics of antiphase boundaries in Fe–Al ordered alloys, Ph.D. thesis, Massachusetts Institute of Technology, Cambridge, MA, 1988. https://dspace.mit.edu/handle/1721.1/54326.
[20] D. Shindo, M.H. Yoo, S. Hanada, K. Hiraga, Direct observation of the shear APB interface in Fe_3Al by HREM, Philos. Mag. A 64 (6) (1991) 1281–1290.
[21] B. Park, G.B. Stephenson, S.M. Allen, K.F. Ludwig Jr., Development of fluctuations into domains during ordering in Fe_3Al, Phys. Rev. Lett. 68 (11) (1992) 1742–1745.
[22] N. Provatas, K. Elder, Phase-Field Methods in Materials Science and Engineering, Wiley-VCH, Weinheim, Germany, 2011.
[23] L.Q. Chen, Phase-field models for microstructure evolution, Annu. Rev. Mater. Res. 32 (1) (2002) 113–140.
[24] Y. Wang, J. Li, Phase field modeling of defects and deformation, Acta Mater. 58 (4) (2010) 1212–1235.
[25] D.A. Cogswell, W.C. Carter, Thermodynamic phase-field model for microstructure with multiple components and phases: the possibility of metastable phases, Phys. Rev. E 83 (6) (2011) 061602.

[26] J.E. Krzanowski, S.M. Allen, Solute-drag effects at migrating diffuse interfaces—I. Theoretical analysis and application to apbs in Fe–Al alloys, Acta Metall. 34 (6) (1986) 1035–1044.
[27] J.E. Krzanowski, S.M. Allen, Solute-drag effects at migrating diffuse interfaces—II. Experimental investigation of APB migration kinetics and comparison to theory, Acta Metall. 34 (6) (1986) 1045–1050.
[28] M.I. Mendelev, D.J. Srolovitz, A regular solution model for impurity drag on a migrating grain boundary, Acta Mater. 49 (4) (2001) 589–597.
[29] M. Hillert, Solute drag in grain boundary migration and phase transformations, Acta Mater. 52 (18) (2004) 5289–5293.
[30] S.G. Kim, Y.B. Park, Grain boundary segregation, solute drag and abnormal grain growth, Acta Mater. 56 (15) (2008) 3739–3753.
[31] Y. Koizumi, S.M. Allen, Y. Minamino, Solute and vacancy segregation to a/4⟨111⟩ and a/2⟨100⟩ antiphase domain boundaries in Fe_3Al, Acta Mater. 56 (19) (2008) 5861–5874.
[32] Y. Koizumi, S.M. Allen, Y. Minamino, Effects of solute and vacancy segregation on migration of a/4⟨111⟩ and a/2⟨100⟩ antiphase boundaries in Fe_3Al, Acta Mater. 57 (10) (2009) 3039–3051.
[33] Y. Koizumi, S.M. Allen, M. Ouchi, Y. Minamino, Evaluation of ordering mobility from antiphase boundary mobility in Fe_3Al using phase-field simulation, ISIJ Int. 52 (9) (2012) 1678–1682.
[34] R. Smoluchowski, Theory of grain boundary motion, Phys. Rev. 83 (1) (1951) 69–70.
[35] S.G. Cupschalk, N. Brown, Kinetics of antiphase domain growth, Acta Metall. 16 (5) (1968) 657–666.
[36] S.M. Allen, R.W. Balluffi, W.C. Carter, Kinetics of Materials, John Wiley & Sons, Inc., Hoboken, New Jersey, 2005.
[37] J.W. Cahn, J.E. Hilliard, Free energy of a nonuniform system. I. Interfacial free energy, J. Chem. Phys. 28 (2) (1958) 258–267.
[38] S.M. Allen, J.W. Cahn, A microscopic theory for antiphase boundary motion and its application to antiphase domain coarsening, Acta Metall. 27 (6) (1979) 1085–1095.
[39] M. Salamon, D. Fuks, H. Mehrer, Interdiffusion and Al self-diffusion in iron-aluminides, Defect Diffus. Forum 237 (2005) 444–449.
[40] J.W. Cahn, The impurity-drag effect in grain boundary motion, Acta Metall. 10 (9) (1962) 789–798.
[41] M. Hillert, A model-based continuum treatment of ordering and spinodal decomposition, Acta Mater. 49 (13) (2001) 2491–2497.
[42] M. Sakai, D.E. Mikkola, The growth of antiphase domains in Cu_3Au as studied by transmission electron microscopy, Metall. Trans. 2 (1971) 1635–1641.
[43] H.E. Schaefer, R. Würschum, M. Sob, T. Zak, W.Z. Yu, W. Eckert, F. Banhart, Thermal vacancies and positron-lifetime measurements in $Fe_{76.3}Al_{23.7}$, Phys. Rev. B 41 (17) (1990) 11869.
[44] J. Wolff, M. Franz, A. Broska, B. Köhler, Th. Hehenkamp, Defect types and defect properties in FeAl alloys, Mater. Sci. Eng. A 239–240 (1997) 213–219.
[45] S.M. Kim, D.G. Morris, Long range order and vacancy properties in Al-rich Fe_3Al and Fe_3Al(Cr) alloys, Acta Mater. 46 (8) (1998) 2587–2602.
[46] P.L. Rossiter, The Electrical Resistivity of Metals and Alloys, 6, Cambridge University Press, 1991.
[47] R. Kerl, J. Wolff, T. Hehenkamp, Equilibrium vacancy concentrations in FeAl and FeSi investigated with an absolute technique, Intermetallics 7 (3–4) (1999) 301–308.
[48] F.C. Nix, W. Shockley, Order-disorder transformations in alloys, Rev. Mod. Phys. 10 (1) (1938) 1.
[49] T. Muto, Y. Takagi, The theory of order-disorder transitions in alloys, Solid State Phys. 1 (1955) 193–282.
[50] J.L. O'brien, G.C. Kuczynski, X-ray study of the kinetics of ordering in AuCu, Acta Metall. 7 (12) (1959) 803–806.
[51] K. Rudisch, A. Davydova, C. Platzer-Björkman, J. Scragg, The effect of stoichiometry on Cu-Zn ordering kinetics in Cu_2ZnSnS_4 thin films, J. Appl. Phys. 123 (16) (2018) 161558.
[52] R. Kozubski, M.C. Cadeville, In situ resistometric investigation of ordering kinetics in Ni_3Al, J. Phys. F 18 (12) (1988) 2569–2575.
[53] R. Kozubski, J. Sołtys, M.C. Cadeville, V. Pierron-Bohnes, T.H. Kim, P. Schwander, J.P. Hahn, G. Kostorz, J. Morgiel, Long-range ordering kinetics and ordering energy in Ni_3Al-based γ' alloys, Intermetallics 1 (3) (1993) 139–150.
[54] F.E. Spada, F.T. Parker, C.L. Platt, J.K. Howard, X-ray diffraction and Mössbauer studies of structural changes and $L1_0$ ordering kinetics during annealing of polycrystalline $Fe_{51}Pt_{49}$ thin films, J. Appl. Phys. 94 (8) (2003) 5123–5134.
[55] B. Rellinghaus, E. Mohn, L. Schultz, T. Gemming, M. Acet, A. Kowalik, B.F. Kock, On the $L1_0$ ordering kinetics in Fe-Pt nanoparticles, IEEE Trans. Magn. 42 (10) (2006) 3048–3050.
[56] F. Seitz, On the theory of diffusion in metals, Acta Crystallogr. 3 (5) (1950) 355–363.
[57] P. Fahey, S.S. Iyer, G.J. Scilla, Experimental evidence of both interstitial and vacancy assisted diffusion of Ge in Si, Appl. Phys. Lett. 54 (9) (1989) 843–845.
[58] R. Van Gastel, E. Somfai, S.B. Van Albada, W. Van Saarloos, J.W.M. Frenken, Vacancy diffusion in the Cu (001) surface I: an STM study, Surf. Sci. 521 (1–2) (2002) 10–25.
[59] A. Van der Ven, H.C. Yu, G. Ceder, K. Thornton, Vacancy mediated substitutional diffusion in binary crystalline solids, Prog. Mater. Sci. 55 (2) (2010) 61–105.
[60] A. Kostka, D. Naujoks, T. Oellers, S. Salomon, C. Somsen, E. Öztürk, A. Savan, A. Ludwig, G. Eggeler, Linear growth of reaction layer during in-situ TEM annealing of thin film Al/Ni diffusion couples, J. Alloys Compd. 922 (2022) 165926.
[61] S.O. Akintunde, P.A. Selyshchev, The influence of radiation-induced vacancy on the formation of thin-film of compound layer during a reactive diffusion process, J. Phys. Chem. Solids 92 (2016) 64–69.
[62] H. Mehrer, Diffusion in intermetallics, Mater. Trans., JIM 37 (6) (1996) 1259–1280.
[63] M. Eggersmann, H. Mehrer, Diffusion in intermetallic phases of the Fe–Al system, Philos. Mag. A 80 (5) (2000) 1219–1244.
[64] K. Elphick, W. Frost, M. Samiepour, T. Kubota, K. Takanashi, H. Sukegawa, S. Mitani, A. Hirohata, Heusler alloys for spintronic devices: review on recent development and future perspectives, Sci. Technol. Adv. Mater. 22 (1) (2021) 235–271.
[65] T. Bachaga, J. Zhang, M. Khitouni, J.J. Sunol, NiMn-based Heusler magnetic shape memory alloys: a review, Int. J. Adv. Manuf. Technol. 103 (5) (2019) 2761–2772.